*Journal of Clinical and Translational Hepatology* **2026** vol. 14(5) | 511–524
DOI: 10.14218/JCTH.2025.00709

Original Article

# Metabolic Dysfunction-associated Steatotic Liver Disease Diminishes the Efficacy of miR-125b-5p-engineered MSC Therapy for Hepatocellular Carcinoma via HK2 Upregulation: A Multimodal Theranostic Study

Lishan Shen[1#], Xiaowen Luo[1#], Xiaorui Su[2], Xiang Zhou[1], Fengyun Zou[1], Shuangshuang Zhong[1], Yayin Deng[1], Boya Yin[1], Zhicheng Yao[2*] and Ruomi Guo[1*]

*[1]Department of Radiology, The Third Affiliated Hospital of Sun Yat-Sen University, Guangzhou, Guangdong, China; [2]Department of Hepatobiliary-Pancreatic-Splenic Surgery, The Third Affiliated Hospital of Sun Yat-Sen University, Guangzhou, Guangdong, China*

**Received:** December 31, 2025 | **Revised:** February 07, 2026 | **Accepted:** April 16, 2026 | **Published online:** May 11, 2026

## Abstract

***Background and Aims:*** Hepatocellular carcinoma (HCC) remains a leading cause of cancer-related mortality, underscoring the need for effective therapies. Although miR-125b-5p shows therapeutic potential, its efficacy in metabolic dysfunction-associated steatotic liver disease (MASLD)-related HCC and the underlying mechanisms remain unclear. In this study, we aimed to develop a magnetic resonance imaging (MRI)-trackable miR-125b-5p-engineered MSC platform for HCC therapy and to determine whether MASLD attenuates its antitumor efficacy through metabolic reprogramming. ***Methods:*** Bone marrow mesenchymal stem cells (MSCs) were genetically engineered to coexpress miR-125b-5p (a therapeutic gene) and ferritin heavy chain (Fth; a MRI reporter gene), enabling sustained delivery and real-time tracking. Orthotopic HCC models with or without MASLD were established to evaluate therapeutic outcomes. In vivo MRI, histological analyses, and bioinformatics approaches were used to assess efficacy and mechanisms. ***Results:*** Transplantation of miR-125b-5p-Fth-MSCs significantly suppressed HCC growth in vivo over an extended period. However, MASLD attenuated this therapeutic effect. Mechanistically, miR-125b-5p directly targeted hexokinase 2 (HK2), inhibiting HCC proliferation and migration through suppression of the PI3K/AKT/mTOR pathway. Fatty acid-induced lipotoxicity upregulated HK2 expression and counteracted the antitumor effects of miR-125b-5p. ***Conclusions:*** Multigene-modified MSCs enable effective, MRI-monitored HCC therapy. MASLD diminishes the efficacy of miR-125b-5p through HK2 upregulation. These findings establish a multimodal theranostic framework for HCC and provide mechanistic insights into MASLD-associated therapeutic resistance.

**Citation of this article:** Shen L, Luo X, Su X, Zhou X, Zou F, Zhong S, *et al*. Metabolic Dysfunction-associated Steatotic Liver Disease Diminishes the Efficacy of miR-125b-5p-engineered MSC Therapy for Hepatocellular Carcinoma via HK2 Upregulation: A Multimodal Theranostic Study. J Clin Transl Hepatol 2026;14(5):511–524. doi: 10.14218/JCTH.2025.00709.

## Introduction

Hepatocellular carcinoma (HCC) accounts for approximately 85% of primary liver cancers and remains a major global health burden, with an increasing incidence worldwide.[1] In 2020, liver cancer was the sixth most commonly diagnosed malignancy and the third leading cause of cancer-related death, with approximately 906,000 new cases and 830,000 deaths. The highest incidence rates are observed in East Asia, Southeast Asia, and North and Western Africa, although the burden is also increasing in Western countries because of the increasing prevalence of metabolic risk factors.[2] Curative options such as resection and ablation are reserved for early-stage disease, whereas intermediate- and advanced-stage HCC require transcatheter arterial chemoembolization and systemic therapies, respectively.[3] Despite treatment advances, HCC remains the third leading cause of cancer-related death worldwide, and the relative five-year survival rate is only approximately 18%, largely because of poor outcomes in advanced disease.[2]

Key factors driving HCC progression, recurrence, and therapeutic resistance include cancer stem cells, an immunosuppressive microenvironment, and metabolic reprogramming.[4] Accordingly, strategies targeting cancer stem cells and enhancing antitumor immunity have attracted increasing interest.[5] Among emerging therapeutic candidates, microRNAs (miRNAs), a class of evolutionarily conserved noncoding

---

**Keywords:** Hepatocellular carcinoma; Nonalcoholic fatty liver disease; miR-125b-5p; Mesenchymal stem cell; Magnetic resonance imaging; HK2.

[#] Contributed equally to this work.

[*] **Correspondence to:** Ruomi Guo, Department of Radiology, The Third Affiliated Hospital of Sun Yat-Sen University, 600 Tianhe Road, Guangzhou, Guangdong 510630, China. ORCID: https://orcid.org/0000-0002-8207-8746. Tel: +86-20-85253108, E-mail: guoruomi86@mail.sysu.edu.cn. Zhicheng Yao, Department of Hepatobiliary-Pancreatic-Splenic Surgery, The Third Affiliated Hospital of Sun Yat-Sen University, No. 600 Tianhe Road, Guangzhou, Guangdong 510630, China. ORCID: https://orcid.org/0000-0001-6668-3922. Tel: +86-20-85253161, E-mail: yaozhch2@mail.sysu.edu.cn.

RNAs that regulate oncogenic pathways at the posttranscriptional level, have received considerable attention.[6] Notably, miR-125b-5p has been shown to suppress proliferation, metastasis, and stemness in multiple malignancies, including HCC.[7]

However, effective gene delivery remains a major challenge. Stem cell–based therapy has become an important focus of preclinical HCC research.[8] Bone marrow–derived mesenchymal stem cells (MSCs) represent attractive delivery vehicles because of their low immunogenicity, high accessibility, and ease of expansion without major ethical concerns.[9] Nevertheless, the limited therapeutic paracrine activity of conventional MSCs has restricted their broader application.[10] To overcome these limitations, the use of MSCs as vectors for gene therapy has emerged as a promising strategy. Unlike single-dose nanomaterial–based delivery systems, MSCs can survive in vivo and continuously release therapeutic factors, thereby functioning as a sustained-release carrier.[11]

In addition, real-time monitoring of MSC fate and their therapeutic effects is crucial for optimizing treatment protocols and evaluating efficacy. Magnetic resonance imaging (MRI) offers distinct advantages for the assessment of liver disease.[12] Ferritin heavy chain (Fth), an MRI reporter gene, decreases T2-weighted imaging (T2WI) signal intensity through its ferroxidase activity,[13] thereby enabling noninvasive, real-time monitoring of stem cell transplantation, migration, and survival.[14] Furthermore, synthetic MRI (SyMRI) is a novel quantitative magnetic resonance technique that simultaneously generates T1, T2, and proton density (PD) maps in a single scan.[15] Compared with normal tissue or low-grade malignancies, tumors, particularly high-grade tumors, generally exhibit higher T1 and T2 values,[16] allowing SyMRI to precisely evaluate iron content and treatment response. Additionally, the proton density fat fraction (PDFF) is a noninvasive method that generates a fat fraction map to quantitatively measure fat deposition in organs.[17]

The global incidences of obesity and metabolic syndrome have paralleled a rise in HCC attributable to metabolic dysfunction-associated steatohepatitis (MASH), now exceeding that linked to viral hepatitis.[18] Recent evidence further suggests that immunotherapy is less effective in metabolic dysfunction-associated steatotic liver disease (MASLD)-related HCC than in viral hepatitis-related HCC.[19,20] These findings raise the possibility that MASLD may also impair the efficacy of miRNA-based treatments for HCC.

Despite growing evidence linking MASLD to inferior immunotherapy response, the effect of MASLD-associated metabolic dysregulation on miRNA-based therapies remains unclear. Specifically, whether and how hepatic steatosis attenuates the antitumor effects of miR-125b-5p in HCC has not been investigated. Moreover, although MSCs have been explored as delivery vehicles for multiple therapeutic genes, no previous study has combined miR-125b-5p delivery with Fth-based MRI monitoring in MASLD-associated HCC.

Herein, we engineered MSCs to codeliver miR-125b-5p and Fth, thereby integrating treatment with imaging surveillance. We investigated the antitumor efficacy of miR-125b-5p in HCC and examined how MASLD-associated metabolic dysregulation attenuates this therapeutic effect, with particular focus on the miR-125b-5p/HK2 axis and the downstream PI3K/AKT/mTOR signaling pathway. By addressing this knowledge gap, our findings may inform therapeutic stratification and optimization for the growing population of HCC patients arising in the setting of MASLD.

## Methods

### Polyplex synthesis and characterization

Polyethylene glycol-polyethylenimine (PEG-PEI) copolymer was synthesized as previously described, and its structure was confirmed by $^1$H nuclear magnetic resonance ($^1$H-NMR).[21] DNA/miRNA-loaded PEG-PEI nanopolyplexes were prepared at an N/P ratio of 15 by mixing PEG-PEI with plasmids/miRNA in 0.9% sodium chloride solution, followed by vortexing and incubation at room temperature for 15 min. Hydrodynamic size and zeta potential were measured using a Zetasizer, and morphology was observed by scanning electron microscopy, and the cytotoxicity of PEG-PEI in MSCs was assessed using a Cell Counting Kit-8 (CCK-8; Dojindo, Japan) assay.

### MSC transfection and characterization

Mouse bone marrow–derived MSCs (iCELL Bioscience Inc., Shanghai, China) were transfected with polyplexes and assigned to four groups: miR-125b-5p+Fth+MSCs (miR-Fth-MSCs), Fth+MSCs (Fth-MSCs), miR-125b-5p+MSCs (miR-MSCs), and untreated MSCs (MSCs). Surface antigen expression (Sca-1, CD90, CD105, CD34, CD45) and apoptosis were evaluated by flow cytometry using established protocols.[4,10]

Cell viability was assessed by trypan blue exclusion and CCK-8 assays, as previously described.[10] For trypan blue staining, MSCs were mixed with 0.4% trypan blue (Sigma-Aldrich) and counted using a hemocytometer. For the CCK-8 assay, cells were seeded in 96-well plates at 5,000 cells/well, incubated for 24, 48, and 72 h, and absorbance at 450 nm was measured after addition of CCK-8 reagent.

Migration capacity was determined by Transwell and wound-healing assays and quantified using ImageJ, as previously described.[11] For Transwell migration, $2 \times 10^5$ MSCs in serum-free DMEM were added to the upper chamber (8-μm pores), with complete medium containing 10% FBS in the lower chamber. After 36 h, migrated cells on the lower surface were fixed, stained with 0.1% crystal violet, and counted. For the wound-healing assay, confluent MSCs were scratched with a pipette tip, washed, and cultured in serum-free medium; wound closure was observed at 0, 12, and 36 h.

MSC differentiation was induced using commercial media (Procell) according to the manufacturer's instructions, as previously described.[10] MSCs were seeded at $2 \times 10^4$ cells/cm$^2$ and cultured in osteogenic or adipogenic differentiation medium for 21 days, with medium changed every three days. Differentiated cells were fixed with 4% formaldehyde and stained with Oil Red O or Alizarin Red S, respectively.

Gene and protein expression were analyzed by RT-qPCR and Western blot (WB), respectively, using previously reported procedures.[10]

### Iron accumulation assessment

Cells were incubated with ferric ammonium citrate (FAC) for 72 h. Iron accumulation was examined by Prussian blue staining, atomic absorption spectrometry (AAS), and transmission electron microscopy (TEM). For in vitro MRI, $1 \times 10^6$ cells were suspended in 4% agarose gel and scanned on a clinical 3.0-T scanner (Signa Architect, GE Healthcare) using T1WI, T2WI, and T2 mapping sequences, as previously described.[14]

### Isolation and characterization of MSC-derived exosomes (MSC-Exos)

MSC-Exos were isolated from conditioned media by sequential centrifugation (300 × g, 2,000 × g, and 10,000 × g), filtration through a 0.22-μm filter, and ultracentrifugation at 100,000 × g for 180 min, as previously described.[10] Exosome characteristics were analyzed by TEM, nanoparticle tracking analysis, and WB for CD9, TSG101, and calnexin. For uptake studies, exosomes were labeled with PKH-26 and visualized by confocal microscopy. The effects of MSC-Exos on liver cancer cells were assessed in vitro and in vivo using migration and apoptosis assays as described above.[10]

### *Animal models*

All animal experiments were approved by the Institutional Animal Care and Use Committee. Male BALB/c-nu nude mice (6 weeks, 20–25 g) and Sprague-Dawley (SD) rats (8 weeks, 200–250 g) were obtained from Sun Yat-sen University Animal Experiment Center.

MASLD models were established in Sprague-Dawley rats by high-fat diet combined with carbon tetrachloride gavage for 8, 10, and 12 weeks, respectively, resulting in mild (5%–33% steatosis), moderate (33%–66%), and severe (>66%) steatosis, confirmed by body weight, PDFF measurements, Hematoxylin and eosin (H&E) staining, Oil Red O, and Masson's trichrome staining, as previously described.[4]

Orthotopic HCC models were generated by inoculating luciferase-expressing HUH7 cells into BALB/c-nu nude mice and Sprague-Dawley rats. Tumor growth was monitored using IVIS Spectrum.[4]

### *MSC transplantation and treatment protocol*

Tumor-bearing mice were randomly assigned to six groups (n = 5 each) and received via portal vein injection: $1 \times 10^6$ miR-Fth-MSCs, Fth-MSCs, miR-MSCs, MSCs, miR-Fth-MSC-Exos, or PBS. Rat groups received miR-MSC treatment. For the subcutaneous tumor model, nude mice were injected with $5 \times 10^6$ oe-HK2 or oe-NC HUH7 cells; when the tumor volume reached 300 $mm^3$, mice received intravenous miR-MSCs.[11]

### *In vivo MRI*

MRI was performed at baseline and on days 5, 10, 15, and 20 post-transplantation using a clinical 3.0-T scanner with dedicated small-animal coils (WK607, Magtron Inc., Jiangyin, China). T2-weighted imaging, SyMRI (MAGiC sequence; T1, T2, and PD maps), and PDFF (IDEAL IQ sequence) were acquired to evaluate cell survival, distribution, and therapeutic effects. Region of interest analysis was performed to measure T1, T2, and PD values, as previously described.[17,22]

### *Histological and immunohistochemical analyses*

At 20 days after transplantation, liver tissues were harvested, paraffin-embedded, and sectioned (5 μm). H&E staining, Prussian blue staining, and TUNEL assays were performed. Immunohistochemistry was conducted for p21, cleaved caspase-3, Bcl-2, and Bax (1:200, Abcam) with DAB visualization. Whole-slide images were acquired (Pannoramic MIDI, 3DHISTECH) and analyzed using ImageJ software, as previously described.[4]

### *Biochemical assays and biosafety assessment*

Liver tissue cholesterol content was quantified using a cholesterol quantification kit (Abcam). Reactive oxygen species (ROS), malondialdehyde (MDA), and interleukin (IL)-6 were measured using ELISA kits (Abcam). mRNA expression of MCP-1, IL-1β, and TNF-α was determined by RT-qPCR. Liver and kidney function were evaluated by serum ALT, AST, BUN, and Cr, as previously described.[4]

### *Cell coculture assay*

HUH7 cells were cultured with miR-MSCs in conditioned media representing hepatocytes with different degrees of steatosis using Transwell inserts (3-μm pore size). Apoptosis of HUH7 cells was then assessed by flow cytometry (Annexin V-FITC/PI staining) using established methods.[10]

### *Bioinformatics analysis*

Potential targets of miR-125b-5p were predicted using miRDB (http://www.mirdb.org), TargetScan (http://www.targetscan.org), and miRTarBase (https://bio.tools/mirtarbase). Gene Ontology (GO) and Kyoto Encyclopedia of Genes and Genomes (KEGG) pathway enrichment analyses were performed using the clusterProfiler R package.[23]

### *Dual-luciferase reporter assay*

HUH7 cells were co-transfected with luciferase reporter plasmids containing wild-type or mutant 3′ UTR of HK2 together with miR-125b-5p mimics or negative controls using Lipofectamine™ 3000. Luciferase activity was measured using a dual-luciferase reporter assay system, as previously described.[24]

### *Gene transfection and functional assays in HUH7 cells*

Lentiviral vectors containing miR-125b-5p mimic, miR-125b-5p inhibitor, HK2 overexpression construct, and corresponding controls were transfected into HUH7 cells using Lipofectamine™ 3000. Transfection efficiency was assessed by RT-qPCR. Cell proliferation was evaluated using CCK-8 and colony formation assays, and migration was assessed by Transwell and wound-healing assays, as previously described.[7]

### *Induction of lipotoxicity and WB analysis*

To induce lipotoxicity in HUH7 cells, palmitic acid (0.5 mM, Sigma-Aldrich) and oleic acid (1 mM) were dissolved in 0.5% fatty acid-free BSA (BAH66-0100, Equitech Bio) before treatment, and WB analysis was subsequently performed.

### *WB analysis*

Proteins were extracted using RIPA lysis buffer with protease inhibitor, quantified by BCA assay, separated by SDS-PAGE, and transferred to PVDF membranes. Membranes were incubated with primary antibodies against Fth (ab65080, Abcam), GAPDH (5174, Cell Signaling), HK2 (BF0283, Affinity Biosciences), mTOR (AF6309-50), p-mTOR (AF3308), PI3K (AF6241), p-PI3K (AF3241), AKT (AF0836), p-AKT (AF0016), and β-actin (AF7018), followed by HRP-conjugated secondary antibodies. Protein signals were visualized by chemiluminescence and quantified using ImageJ, as previously reported.[10]

### *RT-qPCR*

Total RNA was extracted using TRIzol reagent. cDNA was synthesized using PrimeScript RT Reagent Kit. qPCR was performed using SYBR Green qPCR Super Mix on an ABI PRISM 7500 System. Relative expression was calculated using the $2^{-\Delta\Delta Ct}$ method, with U6 or 18S serving as internal controls, as previously described.[10] Primer sequences are listed in Table 1.

### *Statistical analysis*

Data are presented as mean ± standard deviation. Statistical significance was determined by Student's *t*-test, one-way ANOVA with Bonferroni post-hoc correction, Spearman's rank

**Table 1. Primer sequences used for RT-qPCR analysis**

| Target | Sequence |
|---|---|
| miR-125b-5p | F 5′ ACACTCCAGCTGGGTCCCTGAGACCCTAACT 3′ |
| | R 5′ CTCAACTGGTGTCGTGGA 3′ |
| U6 | F 5′ CTCGCTTCGGCAGCACA 3′ |
| | R 5′ AACGCTTCACGAATTTGCGT 3′ |
| Fth | F 5′ CCATCAACCGCCAGATCAAC 3′ |
| | R 5′ ATCCTGAAGGAAGATTCGGC 3′ |
| 18S | F 5′ CCTGGATACCGCAGCTAGGA 3′ |
| | R 5′ GCGGCGCAATACGAATGCCCC 3′ |
| MCP-1 | F 5′ GAAAGTCTCTGCCGCCCTT 3′ |
| | R 5′ TTGATTGCATCTGGCTGAGCG 3′ |
| TNF-α | F 5′ CATCTTCTCAAAATTCGAGTGACAA 3′ |
| | R 5′ CCCAACATGGAACAGATGAGGGT 3′ |
| IL-1β | F 5′CTGCCCACAGACCTTCCA 3′ |
| | R 5′ GGACCAGACATCACCAAGC 3′ |

F, forward primer; R, reverse primer; RT-qPCR, reverse transcription quantitative polymerase chain reaction; miR-125b-5p, microRNA-125b-5p; Fth, ferritin heavy chain; MCP-1, monocyte chemoattractant protein-1; TNF-α, tumor necrosis factor-α; IL-1β, interleukin-1β.

correlation test, and log-rank test. Statistical analyses were performed with GraphPad Prism 9, with $P < 0.05$ considered statistically significant.

## Results

### *Polyplex synthesis, MSC transfection, and characterization*

PEG-PEI was successfully synthesized, as confirmed by $^1$H-NMR analysis (Fig. 1A). PEG-PEI exhibited low cytotoxicity, with MSC viability maintained at 90.09% after exposure to 8 μg/mL for 48 h (Fig. 1B); therefore, this concentration was used for polyplex formation. At an N/P ratio of 15, the polyplexes displayed a hydrodynamic size of 189.2 ± 3.2 nm, a zeta potential of 8.5 ± 0.7 mV, and a uniform spherical morphology (Fig. 1C). These polyplexes were used to transfect MSCs, generating four groups: MSCs, miR-125b-5p+MSCs, Fth+MSCs, and miR-125b-5p+Fth+MSCs.

Transfection did not alter MSC surface antigen expression ($CD34^-/CD45^-/Sca\text{-}1^+/CD90^+/CD105^+$), viability (>95%), proliferation, migration, apoptosis (<7%), or osteogenic/adipogenic differentiation capacity (Figs. 1D–G and Supplementary Figs. 1A–D). Transgene expression remained stable, with significant upregulation of Fth and miR-125b-5p in the respective transfected groups (Fig. 1H, $P < 0.0001$). Following FAC incubation, Fth-transfected MSCs exhibited decreased T2WI signal intensity and significantly lower T2 values (109.8 ± 12.54 ms and 109.9 ± 12.6 ms, respectively) compared with untransfected controls (307.8 ± 12.18 ms and 308.9 ± 13.03 ms, $P < 0.0001$) (Fig. 1J). Prussian blue staining, AAS, and TEM confirmed enhanced iron deposition in Fth-expressing MSCs (Fig. 1I and Supplementary Fig. 1E–F), confirming successful reporter gene integration and imaging capability.

### *Inhibition of HCC by miR-125b-5p*

SyMRI quantification revealed that untreated tumor tissue exhibited significantly higher T1, T2, and PD values compared with normal liver tissue ($P < 0.0001$; Fig. 2B and C). Following treatment, T2-weighted imaging revealed sustained hypointensity in tumors receiving miR-Fth-MSCs and Fth-MSCs from Day 5 to Day 20 (Fig. 2D–E), consistent with Prussian blue staining and indicating persistent MSC localization. SyMRI further confirmed that Fth-MSC-treated tumors had significantly lower T1, T2, and PD values than controls through Day 20 (Fig. 2E), indicating that MSCs could be reliably tracked in vivo.

Therapeutically, tumor volumes decreased over 20 days in the miR-Fth-MSC and miR-MSC groups, whereas tumors in the Fth-MSC, MSC, and PBS groups continued to grow (Fig. 2D). Corresponding SyMRI quantification revealed time-dependent reductions in T1, T2, and PD values in the miR-MSC cohort (Fig. 2E, green line), with significant differences observed for T1 and T2 values across all time points, whereas PD values differed between Days 15–0 and Days 20–0. The lower values in the miR-Fth-MSC group (blue line) compared with miR-MSC (green) and Fth-MSC (yellow) likely reflect the combined effects of Fth and miR-125b-5p. In contrast, MSC treatment alone (orange) produced a neutral effect on tumor growth compared with PBS (red). Notably, a tumor in the miR-MSC group remained relatively stable in size over time (Fig. 2F), with corresponding T1, T2, and PD trends consistent with treatment-responsive tumors (Fig. 2G), supported by the final pathological findings (Supplementary Fig. 2A).

TUNEL and H&E staining further confirmed that increased miR-125b-5p expression in the miR-Fth-MSC and miR-MSC groups was associated with enhanced apoptosis and necrosis ($P < 0.0001$; Fig. 2H). Upregulation of p21 ($P < 0.0001$) and cleaved Caspase-3 ($P < 0.05$; Supplementary Fig. 2B) indicated that activation of miR-125b-5p (in the miR-Fth-MSC and miR-MSC groups) resulted in cell cycle arrest and apoptosis activation. The Bcl-2/Bax ratio determines whether apoptosis is initiated through regulation of mitochondrial membrane permeability, in which Bax is a proapoptotic protein, and Bcl-2 is an anti-apoptotic protein ($P < 0.0001$). Correlation analysis revealed significant associations between decreased SyMRI parameters and increased TUNEL staining, p21, cleaved Caspase-3, and Bax/Bcl-2 ratio (Supplementary

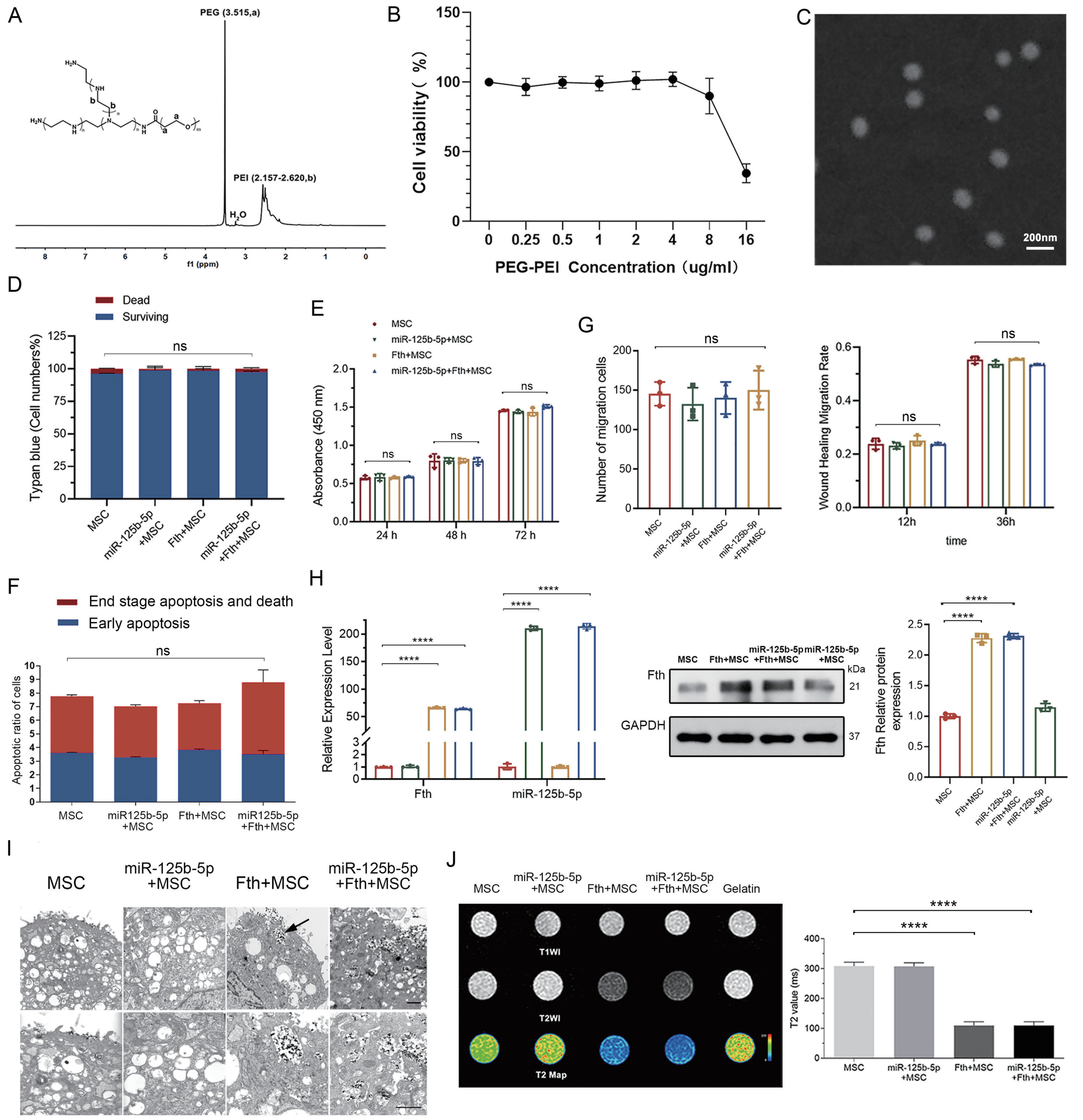

**Fig. 1. Effects of multigene modification on MSC biological activity.** (A) $^1$H-NMR spectra of PEG-PEI. (B) CCK-8 assay of MSC viability after exposure to PEG-PEI at the indicated concentrations. (C) Scanning electron microscopy images of PEG-PEI/miR-125b-5p-Fth nanoparticles at an N/P ratio of 15. (D–G) Assays of MSC viability, proliferation, migration, and apoptosis using trypan blue exclusion, CCK-8, Transwell/wound-healing, and flow cytometry, respectively. (H) RT-qPCR and Western blot analyses of Fth and miR-125b-5p expression in the indicated groups. (I) TEM images of Fth-MSCs and MSCs. (J) In vitro MRI detection of Fth using T1WI, T2WI, and T2 mapping after FAC incubation. Scale bars: 200 nm in C and 1 μm in I. n = 5. ns, not significant; ****$P < 0.0001$. Data are presented as mean ± SD. $^1$H-NMR, Proton nuclear magnetic resonance; CCK-8, Cell Counting Kit-8; FAC, ferric ammonium citrate; MSC, mesenchymal stem cell; PEG-PEI, polyethylene glycol-polyethylenimine; RT-qPCR, reverse transcription quantitative polymerase chain reaction; T1WI, T1-weighted imaging; T2WI, T2-weighted imaging; TEM, transmission electron microscopy.

Fig. 2C). No significant differences in liver or kidney function markers were detected between the MSC and PBS groups, indicating the high biosafety of MSC therapeutic implantation (Supplementary Fig. 3A).

### *Diminished therapeutic effectiveness of miR-125b-5p in rats with a MASLD background*

MASLD models were successfully established, as confirmed by H&E and Oil Red O staining (Supplementary Fig. 3B). None of

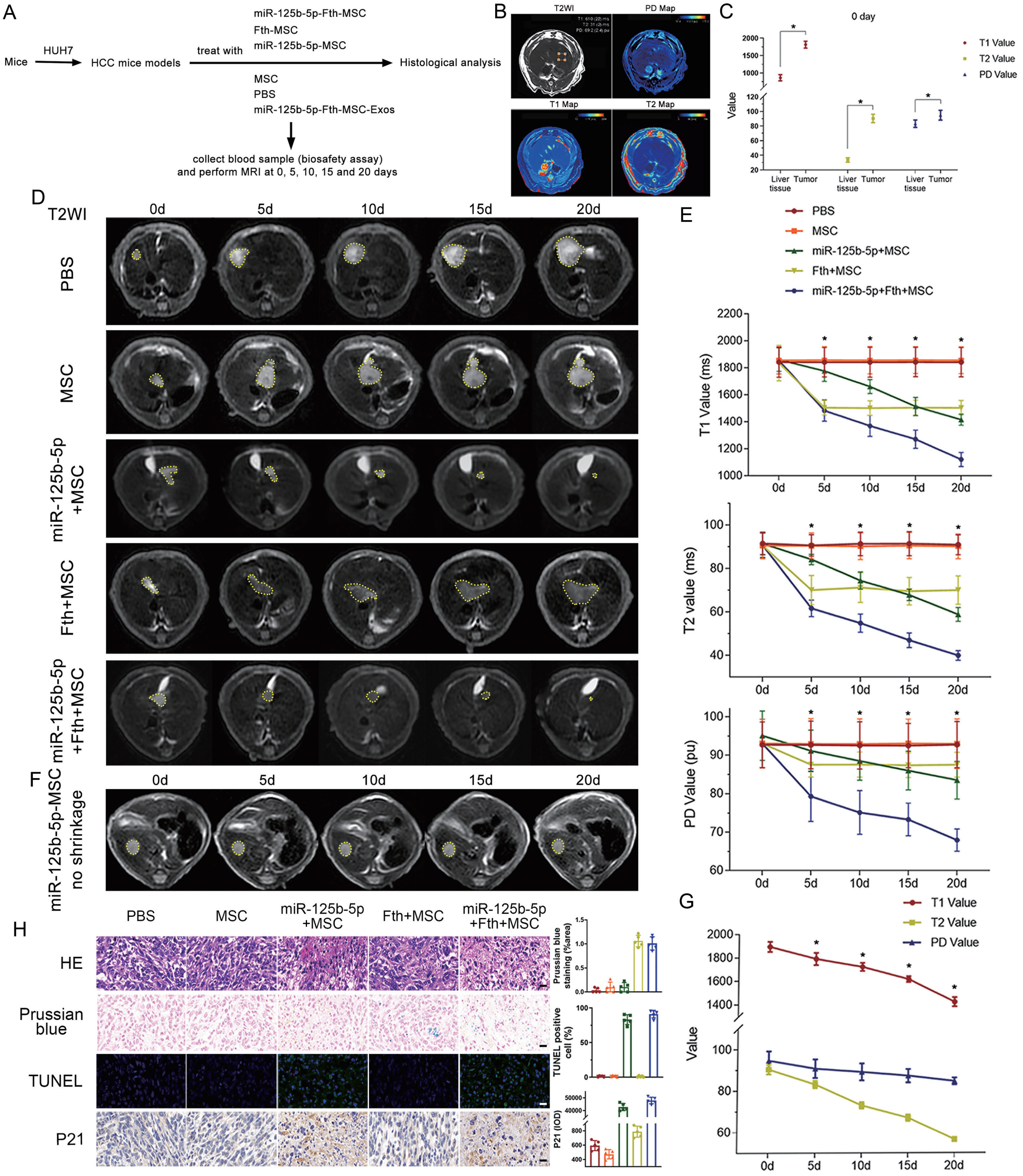

**Fig. 2. Evaluation of miR-125b-5p intervention in an orthotopic liver tumor model.** (A) Experimental design of MSC treatment in the orthotopic HCC model. (B) Representative SyMRI T1, T2, and PD maps with regions of interest drawn for quantification. (C) Baseline SyMRI values in tumor tissue and normal liver tissue. (D) Serial T2WI of orthotopic tumors before and at 5, 10, 15, and 20 days after MSC transplantation. (E) Serial T1, T2, and PD values of tumors in the indicated groups. (F, G) Representative T2WI and quantitative SyMRI values in the miR-125b-5p-MSC group. (H) Representative H&E, Prussian blue, TUNEL, and p21 immunohistochemistry images. Scale bars: 20 μm in H. *$P < 0.05$. Data are presented as mean ± SD. H&E, hematoxylin and eosin; HCC, hepatocellular carcinoma; MSC, mesenchymal stem cell; PD, proton density; SyMRI, synthetic magnetic resonance imaging; T2WI, T2-weighted imaging; TUNEL, terminal deoxynucleotidyl transferase dUTP nick-end labeling.

the groups exhibited liver fibrosis, with an NAS of 5. All groups presented MASLD rather than MASH. Liver tissues were collected for laboratory analysis. miR-125b-5p-MSCs increased HUH7 cell apoptosis after cocultivation, but conditioned media from fatty liver hepatocytes weakened this antitumor response (Fig. 3B). Fatty liver tissues exhibited increased cholesterol deposition (Supplementary Fig. 3C), elevated MDA and ROS levels (Fig. 3B), and progressive expression of IL-6, MCP-1, IL-1β, and TNF-α (Fig. 3B and Supplementary Fig. 3D), indicating oxidative stress and inflammation.

All groups were treated with miR-125b-5p-MSCs and underwent MRI scans before and after treatment; tumor volumes and SyMRI results were measured. On T2WI, the liver signal progressively decreased as fatty liver disease worsened. In contrast, fat fraction maps showed increased liver brightness (Fig. 3C–E). Tumor volumes were significantly larger in the severe fatty liver group at all time points post-treatment ($P < 0.0001$; Fig. 3D), and in the moderate group on Days 10 and 15 ($P < 0.0001$ and $P = 0.002$, respectively), indicating a less effective therapeutic response. On Day 15, the T2 value in the severe fatty liver group was higher than that in the mild fatty liver group ($P = 0.0176$; Fig. 3E), whereas on Day 20, both T1 and T2 values were significantly elevated in the severe group compared with the non- and mild groups (T1: $P = 0.0296$ and $P = 0.0331$; T2: $P = 0.0165$ and $P = 0.0137$; Fig. 3E, Supplementary Fig. 3E and F). Histological findings corroborated these imaging results, demonstrating attenuated apoptosis and cell cycle arrest in MASLD-associated tumors (Fig. 3F and Supplementary Fig. 3G). Therefore, these results indicate that moderate to severe MASLD diminishes the therapeutic efficacy of miR-125b-5p.

### *MSC demonstrates longer-lasting efficacy*

We investigated the effects of MSC-Exos on HCC in vitro and in vivo. MSC-Exos were successfully isolated from conditioned media and characterized by TEM, nanoparticle tracking analysis, and WB. TEM revealed typical biconcave vesicles with diameters around 100 nm (Fig. 4A), while nanoparticle tracking analysis confirmed average particle sizes ranging from 65.51 to 73.38 nm across the four groups (Fig. 4B). WB analysis confirmed positive expression of the exosomal markers CD9 and TSG101, with no calnexin contamination (Fig. 4C). Cellular uptake assessed by confocal microscopy demonstrated efficient internalization of PKH-26-labeled MSC-Exos by HUH7 cells across all groups (Fig. 4D).

The functional effects of different MSC-Exos on HCC cell migration and apoptosis were subsequently assessed in HUH7 cells. In the Boyden chamber migration assay, significantly fewer cells migrated after treatment with miR-125b-5p-containing exosomes (Fig. 4E and Supplementary Fig. 4A), whereas cells not exposed to miR-125b-5p exhibited marked migratory activity through the non-coated porous membrane. Similarly, as illustrated in Figure 4E–F and Supplementary Figure 4A–B, miR-125b-5p treatment inhibited HCC cell migration and enhanced apoptosis. Furthermore, in vivo MR images revealed reduced tumor size and decreased T2 signal intensity on Day 5 after miR-Fth-MSC-Exo transplantation, followed by progressive increases from Day 10 onward (Fig. 4G). Corresponding SyMRI quantification showed a significant reduction on Day 5, followed by a gradual increase from Day 10 onward (Fig. 4H).

### *miR-125b-5p directly targets HK2 in HUH7 cells*

The inhibitory effect of miR-125b-5p on HCC prompted us to further explore its therapeutic mechanism. Bioinformatics analysis identified 104 overlapping miR-125b-5p target genes across databases (Fig. 5A). To gain further insights into these 104 genes, we conducted GO and KEGG pathway functional enrichment analyses. Our findings revealed enrichment in "miRNA metabolic process" and association with "MicroRNAs in cancer". Among the 104 genes, 34 were identified as prognostic factors for overall survival in patients with liver hepatocellular carcinoma (LIHC) based on The Cancer Genome Atlas (TCGA) data. Notably, according to GeneCards, HK2 was the only gene related to metabolism. To analyze the effects of miR-125b-5p and HK2 expression on patient survival, we categorized 370 human LIHC patients into high- and low-expression groups. Low miR-125b-5p expression and high HK2 expression were significantly associated with poor overall survival in patients (Fig. 5B). An inverse correlation between miR-125b-5p and HK2 mRNA expression was observed ($P < 0.0001$; Fig. 5C). These preliminary bioinformatics analyses suggest that HK2 is associated with miR-125b-5p and that both are associated with LIHC prognosis. Furthermore, the GEPIA database indicated that HK2 expression was associated with pathways related to fatty acid metabolism, cholesterol homeostasis, glycolysis, and bile acid metabolism (Fig. 5D), supporting its potential role in metabolic regulation in HCC.

### *miR-125b-5p suppresses HCC by targeting HK2*

Building on the above findings, we further investigated the biological significance and underlying mechanism of the miR-125b-5p/HK2 axis in LIHC. RT-qPCR confirmed successful modulation of miR-125b-5p expression by the mimic or inhibitor (Fig. 6A). Cell proliferation was evaluated by CCK-8 assay, and representative colony-formation dishes are provided in Supplementary Figure 5A. Compared with the corresponding control groups, miR-125b-5p overexpression suppressed proliferation, whereas miR-125b-5p inhibition increased proliferation ($P < 0.0001$; Fig. 6B–C and Supplementary Fig. 5A). In rescue experiments, HK2 overexpression attenuated the antiproliferative effect of miR-125b-5p (Fig. 6G); representative colony-formation dishes are shown in Supplementary Figure 5B.

Wound-healing and Transwell assays demonstrated that cell migration was significantly inhibited by the miR-125b-5p mimic ($P < 0.0001$ and $P = 0.0005$, respectively), whereas this effect was reversed by the miR-125b-5p inhibitor ($P < 0.0001$ and $P = 0.0001$, respectively; Fig. 6D and Supplementary Fig. 5C). HK2 overexpression further promoted cell migration (Fig. 6F and Supplementary Fig. 5D). A dual-luciferase reporter assay (Fig. 6E) showed that the miR-125b-5p mimic significantly inhibited the luciferase activity of the HK2-WT reporter ($P = 0.0018$), whereas no change was observed for the HK2-MUT reporter, confirming that miR-125b-5p directly targets HK2 in HUH7 cells.

To further define the downstream mechanism, WB analysis was performed to examine components of the PI3K/AKT/mTOR pathway (Fig. 6H). Reduced HK2 expression in the miR-125b-5p group was accompanied by decreased phosphorylation of PI3K, AKT, and mTOR. In addition, fatty acid-induced lipotoxicity markedly increased total HK2 protein expression in HUH7 cells, whereas treatment with the miR-125b-5p mimic attenuated this effect. Fatty acid exposure also induced phosphorylation of mTOR and its upstream regulators PI3K and AKT, which was likewise reduced by miR-125b-5p overexpression. Finally, in vivo experiments further confirmed that HK2 is a critical downstream mediator of the antitumor effect of miR-125b-5p. Gross images from the subcutaneous tumor model are shown in Supplementary

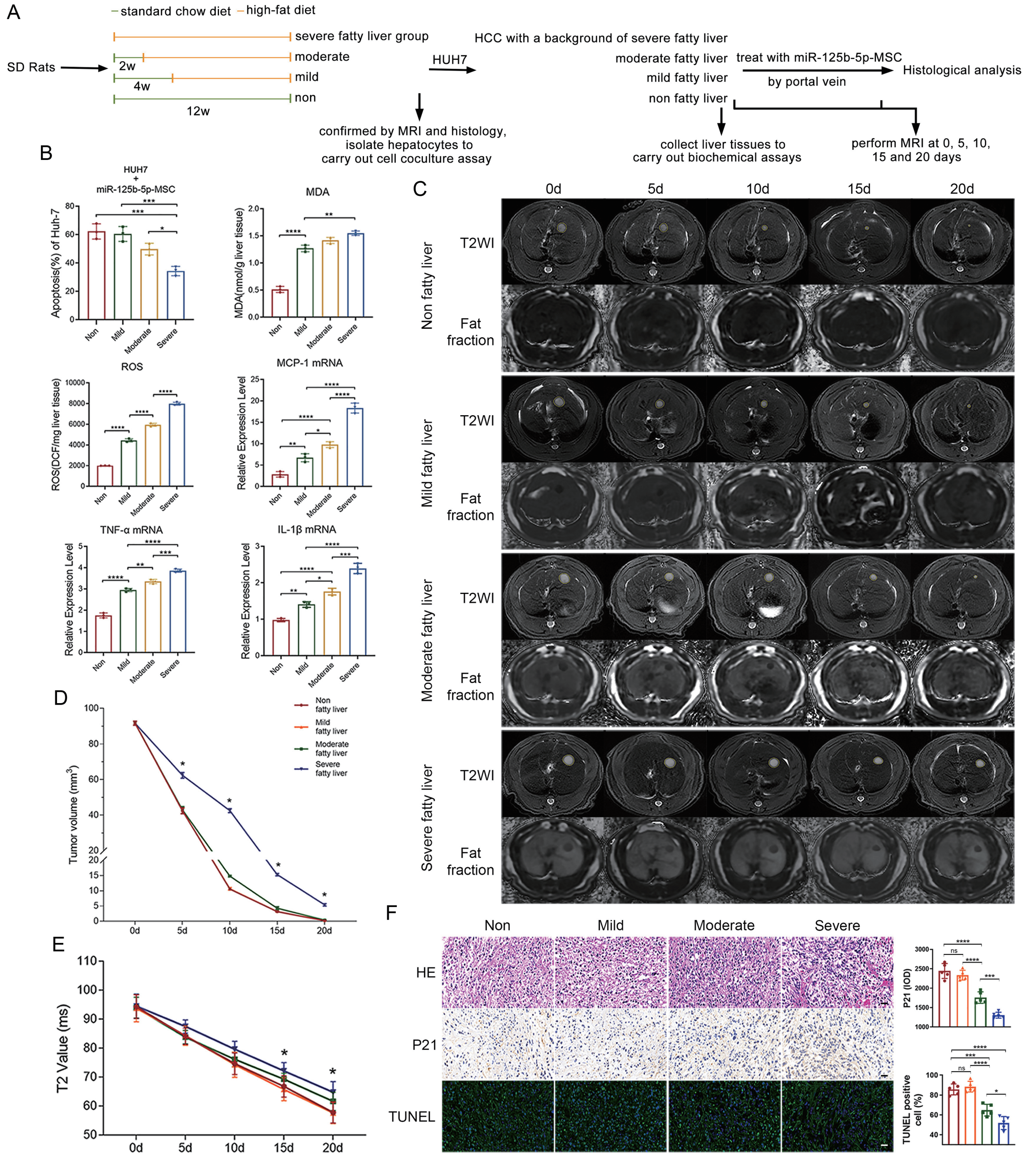

**Fig. 3. Effect of MASLD on the antitumor response to miR-125b-5p.** (A) Experimental design of the MASLD-associated orthotopic HCC study. (B) Coculture assays and measurements of oxidative stress and inflammatory markers, including ROS, MDA, IL-6, MCP-1, IL-1β, and TNF-α, in HUH7 cells exposed to conditioned media from hepatocytes with different degrees of steatosis. (C–E) Serial T2WI, SyMRI, and PDFF assessments before and at 5, 10, 15, and 20 days after miR-125b-5p-MSC transplantation. (F) Representative H&E, p21 immunohistochemistry, and TUNEL images. Scale bars: 20 µm in F. n = 5. ns, not significant; *$P < 0.05$, **$P < 0.01$; ***$P < 0.001$; ****$P < 0.0001$. Data are presented as mean ± SD. H&E, hematoxylin and eosin; HCC, hepatocellular carcinoma; IL-1β, interleukin-1β; IL-6, interleukin-6; MASLD, metabolic dysfunction-associated steatotic liver disease; MCP-1, monocyte chemoattractant protein-1; MDA, malondialdehyde; PDFF, proton density fat fraction; ROS, reactive oxygen species; SyMRI, synthetic magnetic resonance imaging; T2WI, T2-weighted imaging; TNF-α, tumor necrosis factor-α; TUNEL, terminal deoxynucleotidyl transferase dUTP nick-end labeling.

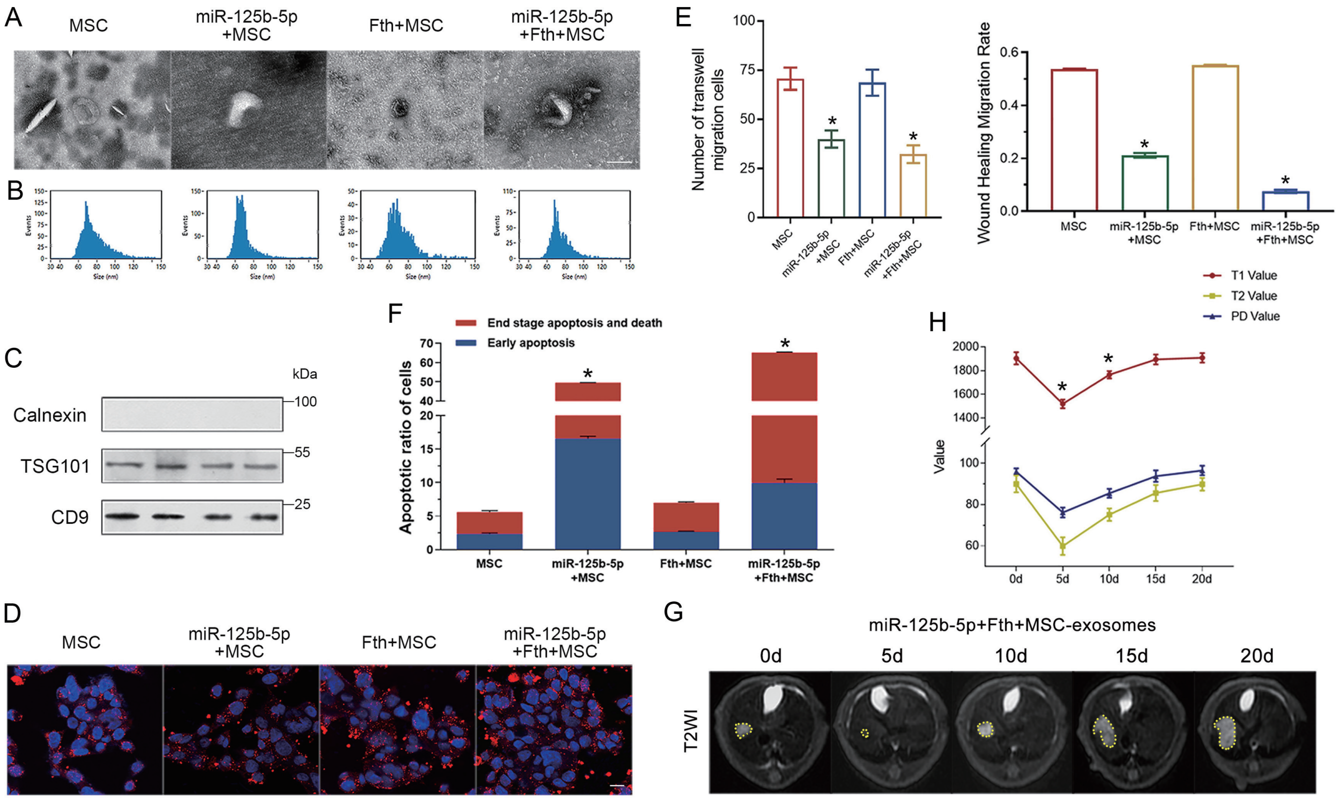

**Fig. 4. Characterization of MSC-Exos and evaluation of their antitumor effects *in vitro* and in an orthotopic HUH7 model.** (A) TEM images of MSC-Exos from the indicated groups. (B) Nanoparticle tracking analysis of MSC-Exo size distribution. (C) Western blot analysis of exosome markers CD9 and TSG101 and the endoplasmic reticulum marker calnexin. (D) Representative confocal microscopy images of HUH7 cells incubated with PKH-26-labeled MSC-Exos (red) and counterstained with DAPI (blue). (E, F) Transwell and wound-healing assays and flow cytometry analysis of HUH7-cell migration and apoptosis after treatment with MSC-Exos from the indicated groups. (G, H) Serial T2WI and quantitative SyMRI values of tumors before and at 5, 10, 15, and 20 days after miR-125b-5p-Fth-MSC-Exos transplantation. Scale bars: 100 nm in A and 20 μm in D. n = 5. **P* < 0.05. Data are presented as mean ± SD. DAPI, 4′,6-diamidino-2-phenylindole; MSC-Exos, mesenchymal stem cell-derived exosomes; SyMRI, synthetic magnetic resonance imaging; T2WI, T2-weighted imaging; TEM, Transmission electron microscopy.

Figure 5E. Moreover, the antitumor effect observed after tail vein injection supports the tumor-targeting capacity of MSC-based delivery.

## Discussion

In this study, we engineered and transplanted miR-125b-5p-Fth-MSCs under MRI guidance, achieving significant suppression of HCC growth through sustained HK2 targeting. Notably, the therapeutic efficacy progressively declined with increasing severity of fatty liver disease, underscoring a critical interaction between tumor metabolism and the hepatic microenvironment.

Previous work revealed that miR-125b-5p potently suppresses HCC progression by targeting TXNRD1,[7] and our findings further support its antitumor potential. Importantly, MASLD-driven HCC is characterized by lipid metabolism abnormalities, mitochondrial dysfunction, and chronic inflammation,[25] which were reflected in our models by increased cytokine production, oxidative stress, and lipotoxicity. Clarifying how these metabolic alterations modulate miR-125b-5p activity is therefore essential. Focusing on metabolic reprogramming,[26] our bioinformatics analyses identified HK2 as the only metabolism-related gene among candidates associated with "microRNAs in cancer". Luciferase reporter assays confirmed HK2 as a direct downstream target of miR-125b-5p. Although the miR-125b-5p/HK2 axis has been reported in other malignancies,[24,27,28] its role in HCC, particularly in the context of MASLD, has not been established. In addition, HK2 is a key regulator of glycolysis,[29] and its increased expression is associated with enhanced glycolytic flux and fibrogenesis in MASLD liver tissue.[30]

Functionally, our data demonstrate that miR-125b-5p suppresses HCC progression by downregulating HK2 and inhibiting the PI3K/AKT/mTOR pathway. Coculture experiments further indicate that the fatty liver microenvironment attenuates the therapeutic efficacy of miR-125b-5p-MSCs. Fatty acid–induced lipotoxicity increased HK2 expression and activated PI3K/AKT/mTOR signaling, partially counteracting miR-125b-5p–mediated effects. These observations are consistent with previous studies showing that inhibition of the PI3K/AKT/mTOR pathway alleviates hepatocyte dysfunction in MASLD.[31] The literature also indicates that miRNAs are key regulators involved in insulin signaling, insulin resistance, fatty acid, triglyceride, lipoprotein, and cholesterol biosynthesis, and MASLD.[32] Cai *et al*. demonstrated that in liver tissues and cells from patients with MASLD, the CpG island in the miR-125b-5p promoter was methylated, resulting in epigenetic silencing of miR-125b-5p.[33] A short-term high-fructose diet was shown to significantly decrease the expression levels of miR-125b-5p in the liver,[32] which may explain the therapeutic suppression we observed. Additionally, miR-125b-5p is dynamically regulated during inflammatory responses, initially decreasing to permit cytokine production

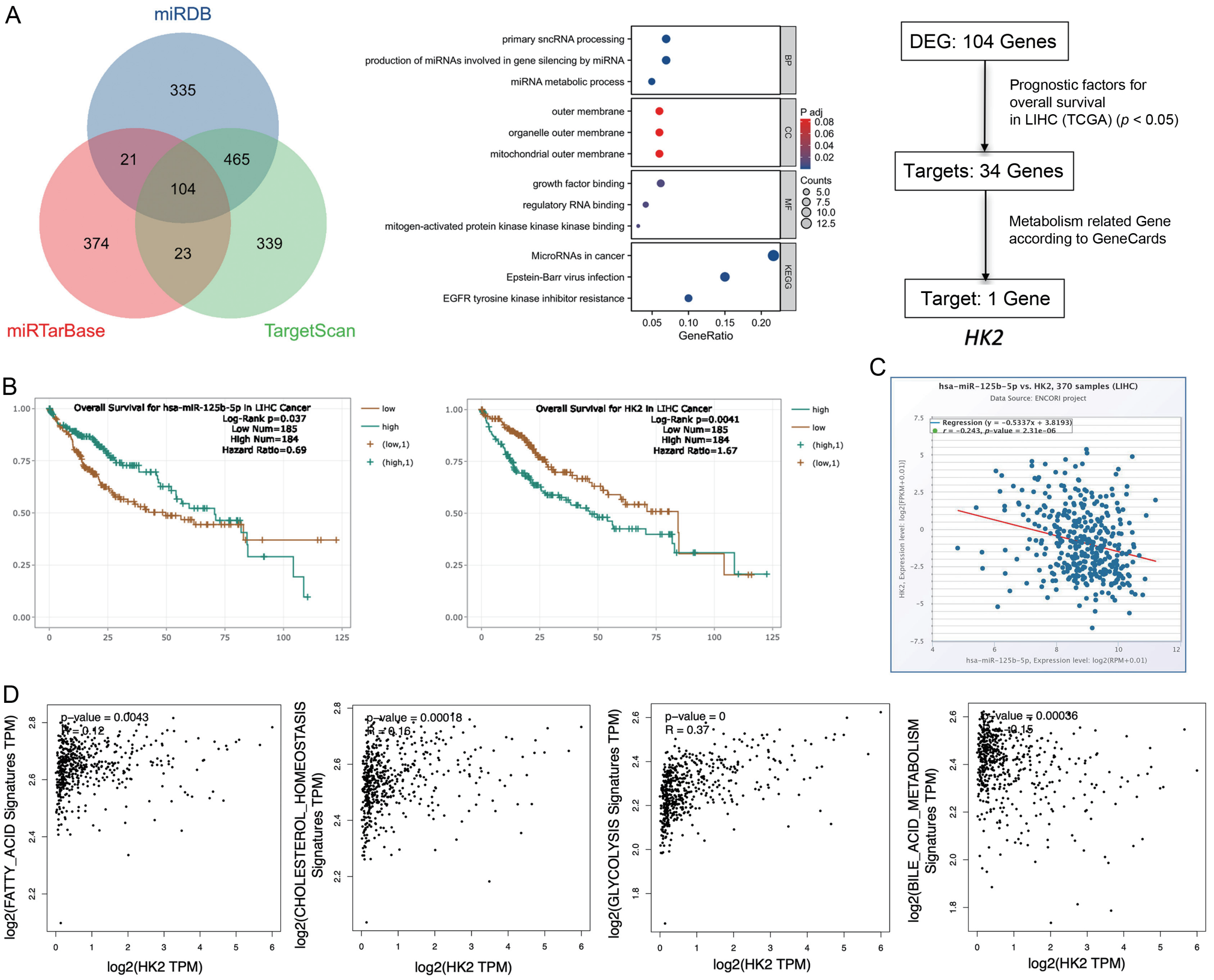

**Fig. 5. Bioinformatics analysis of miR-125b-5p target genes.** (A) Intersection of candidate target genes identified by miRDB, miRTarBase, and TargetScan, followed by GO and KEGG enrichment analyses of the overlapping genes. (B) Kaplan–Meier overall survival curves of 370 LIHC patients stratified by hsa-miR-125b-5p and HK2 expression. (C) Spearman correlation analysis of hsa-miR-125b-5p and HK2 mRNA expression in 370 LIHC samples. (D) Correlation analysis of HK2 with fatty acid metabolism, cholesterol homeostasis, glycolysis, and bile acid metabolism using the GEPIA database. GEPIA, Gene Expression Profiling Interactive Analysis; GO, Gene Ontology; KEGG, Kyoto Encyclopedia of Genes and Genomes; LIHC, liver hepatocellular carcinoma; mRNA, messenger RNA.

and subsequently increasing to limit excessive inflammation.[34] Its expression has also been linked to metabolic regulators such as the vitamin D receptor in adipose tissue.[35] Collectively, these findings support a model in which the MASLD microenvironment imposes a metabolic constraint that diminishes miR-125b-5p–mediated antitumor activity.

Exosomes play a central role in MSC-mediated paracrine signaling and have emerged as promising therapeutic agents because of their small size and low immunogenicity.[36,37] In our experiments, MSC-Exos were internalized by HCC cells and inhibited proliferation and migration while promoting apoptosis. However, their therapeutic effect was transient. The literature indicates that the half-life varies depending on the origin, size, route of administration, or recipient species of extracellular vesicles (EVs). Regardless of the specific EVs, their peak levels in the liver or tumor tissue are generally reached within 48 h, after which levels begin to gradually decrease. By Day 6, they are typically undetectable, which necessitates multiple injections to achieve sustained therapeutic effects.[38] Consistent with this, we observed early tumor regression followed by regrowth after exosome treatment. To prolong the therapeutic duration, we employed MSCs as gene delivery carriers. Previous studies have shown that MSCs can be traced for 28 or 35 days posttransplantation,[11,39] with labeled MSCs detectable up to 90–150 days.[40] Herein, the MSCs acted as cellular "Trojan horses", continuously secreting MSC-Exos to sustain therapeutic delivery for more than 20 days and avoid repeated injections. Furthermore, in vivo experiments on subcutaneous tumors demonstrated the tumor-targeting ability of MSCs. The data published to date show paradoxical effects with respect to MSCs because of their ability to polarize. The level of inflammation and/or the presence of TLR agonists determines whether MSCs polarize toward a proinflammatory/antitumor (MSC1) or an anti-inflammatory/immunosuppressive/protumor (MSC2) phenotype.[41] Some studies suggest that MSCs and their EVs

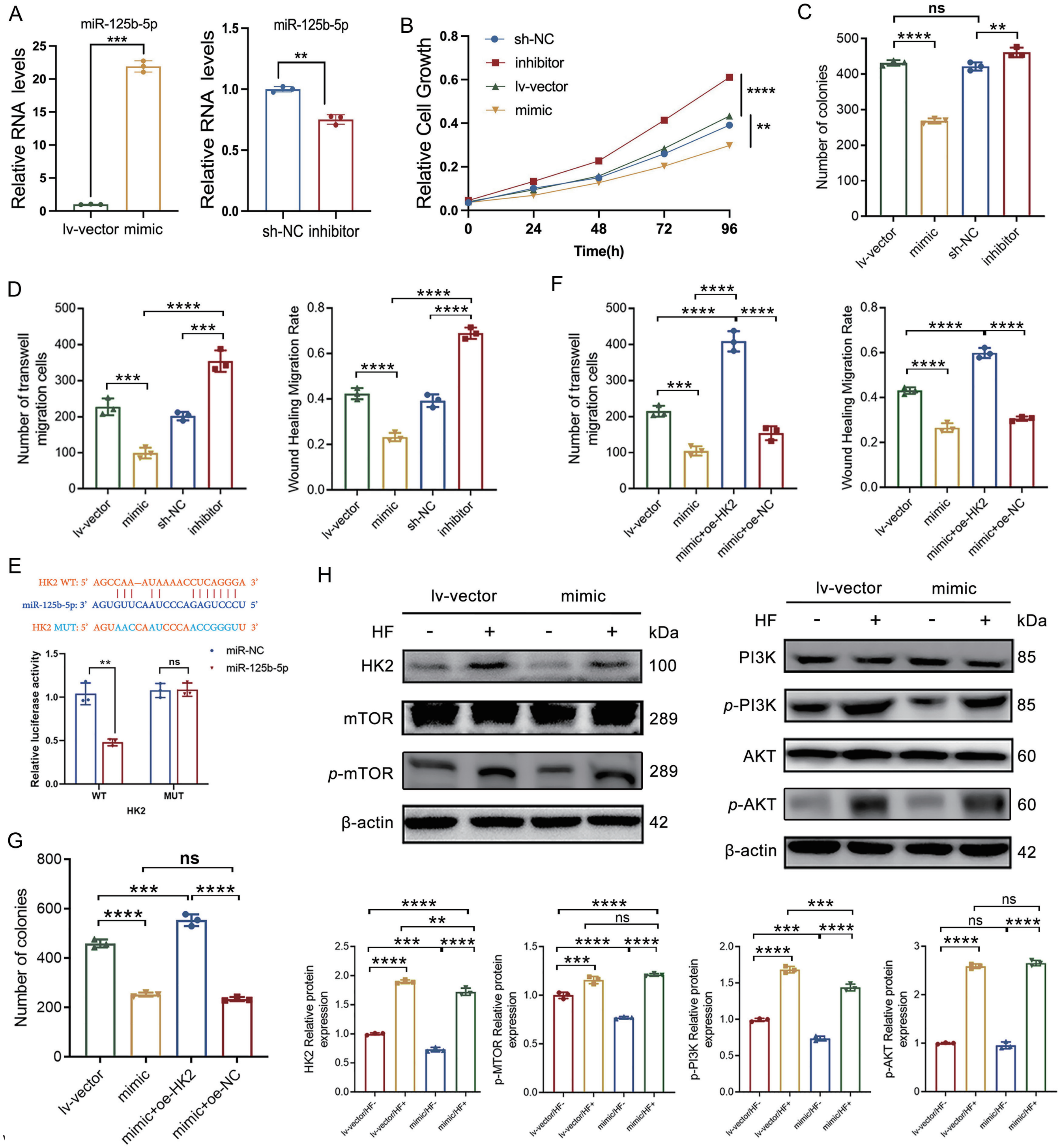

**Fig. 6. Analyses of the miR-125b-5p/HK2 axis in HUH7 cells.** (A) RT-qPCR analysis of miR-125b-5p after transfection with miR-125b-5p mimic, inhibitor, or corresponding controls. (B) CCK-8 assay of HUH7-cell proliferation after miR-125b-5p overexpression or inhibition. (C) Quantification of colony formation after miR-125b-5p overexpression or inhibition; representative colony-formation dishes are shown in Supplementary Figure 5A. (D) Transwell and wound-healing assays of HUH7-cell migration after miR-125b-5p overexpression or inhibition. (E) Schematic of the predicted miR-125b-5p binding sites in the WT and MUT HK2 3′-UTR constructs and dual-luciferase reporter assay results. (F) Transwell and wound-healing assays of HUH7-cell migration after HK2 overexpression; representative images are shown in Supplementary Figures 5C and D. (G) Quantification of colony formation in the HK2 rescue experiment; representative colony-formation dishes are shown in Supplementary Figure 5B. (H) Western blot analysis of HK2, PI3K, p-PI3K, AKT, p-AKT, mTOR, and p-mTOR in HUH7 cells treated with fatty acid and transfected with lv-vector or miR-125b-5p mimic. ns, not significant; **$P < 0.01$; ***$P < 0.001$; ****$P < 0.0001$. Data are presented as mean ± SD. 3′-UTR, 3′ untranslated region; AKT, protein kinase B; CCK-8, Cell Counting Kit-8; lv-vector, lentiviral vector; mTOR, mammalian target of rapamycin; MUT, mutant; p-AKT, phosphorylated AKT; PI3K, phosphoinositide 3-kinase; p-mTOR, phosphorylated mTOR; p-PI3K, phosphorylated PI3K; RT-qPCR, Reverse transcription quantitative polymerase chain reaction; WT, wild-type; -, without; +, with.

tend to exert anti-inflammatory and antifibrotic effects on MASLD, MASH, and liver fibrosis.[42] However, their functional phenotype is influenced by cell source, expansion conditions, dose, and timing of administration.[43] One solution is to use genetically modified MSCs, which have demonstrated promising results against various cancers in animal models.[41,44] In this study, unmodified MSCs exhibited minimal effects on tumor growth, likely due to insufficient dosage and limited intrinsic activity. This limitation was addressed through genetic modification with miR-125b-5p, which enhanced their antitumor efficacy.

A major strength of our study is the multimodal theranostic approach that integrates therapy and imaging. MRI enabled longitudinal tracking of MSC distribution and therapeutic response through Fth-mediated contrast.[45] Unlike conventional SPIO labeling, which is diluted with cell division, the Fth reporter–enabled imaging traits are inherited by MSC progeny via mitosis, allowing long-term tracking.[46] Our results demonstrated that Fth gene-modified MSCs produced detectable contrast differences on MRI, enhancing traceability and diagnostic efficiency. Importantly, Fth overexpression did not affect the proliferation rate of MSCs, which is consistent with previous findings.[47] Another innovative aspect of this study is the application of quantitative SyMRI for early response assessment. Prior SyMRI studies have reported higher T1 and T2 values in rectal tumors than in normal tissue.[16] Additionally, compared with low-grade invasive ductal breast cancer, high-grade invasive ductal breast cancer has markedly elevated T1 and PD values.[48] Moreover, T1 and T2 values are elevated in triple-negative tumors but decreased in non-triple-negative tumors.[22] In our study, we measured T1, T2, and PD values to assess the therapeutic efficacy of miRNA treatment, with reductions in these values indicating effective treatment. Variations in these values before and after treatment can be attributed to intrinsic tissue properties, including water content, microvascular density, proliferation, and other molecular-level microstructural differences.[22,49] Notably, quantitative changes were detectable even in one case without apparent volumetric reduction, suggesting that SyMRI may capture early biological responses preceding macroscopic tumor shrinkage. Although the sample size is limited, this phenomenon is consistent with what we observe in clinical practice. The significant correlations between MRI values and molecular markers of cell cycle arrest (p21) and apoptosis (c-Caspase-3) indicate that T1, T2, and PD relaxation times can serve as surrogate in vivo readouts of underlying therapeutic efficacy. These findings support the clinical potential of quantitative MRI for early response assessment, enabling identification of responders prior to volumetric changes and timely therapy adaptation, which is consistent with the literature.[49] To our knowledge, this is the first demonstration of SyMRI-based early response monitoring in a MASLD-driven HCC model, providing a framework for future clinical translation.

Several limitations exist in this study. First, we established a MASLD model and directly implanted liver cancer cells into this model, rather than progressing from liver fibrosis and cirrhosis to HCC. Despite this limitation, our data revealed increased levels of cytokines, chemokines, and oxidative stress products in the liver, suggesting that the hepatic microenvironment of our HCC model with a fatty liver background resembled that of MASH-related HCC.[50] Future studies employing spontaneous HCC development models in the setting of progressive MASLD/MASH could more accurately recapitulate the evolution of human disease. Second, we did not further validate strategies to overcome resistance in the MASLD model. In future studies, we intend to explore approaches such as combining HK2 inhibitors or modulating lipid metabolism. Third, the clinical translation of MSC-based therapies faces regulatory challenges related to standardization, safety, and regulatory approval.

## Conclusions

This study demonstrated that miR-125b-5p-engineered MSCs exerted potent antitumor effects against HCC through HK2 downregulation and PI3K/AKT/mTOR pathway inhibition, while Fth enabled noninvasive MRI tracking. Importantly, we identified MASLD-associated metabolic dysregulation as a resistance mechanism characterized by HK2 upregulation and PI3K/AKT/mTOR pathway reactivation. These findings have important clinical implications. First, HCC patients with underlying MASLD may require stratified therapeutic approaches rather than being managed identically to other HCC subtypes. Second, combination strategies targeting HK2 or lipid metabolism may be needed to overcome resistance. Finally, quantitative MRI parameters may serve as early biomarkers of treatment response and could facilitate individualized treatment adaptation. Overall, this study provides a foundation for the rational design of MSC-based theranostic strategies for HCC while emphasizing the importance of host metabolic status in therapeutic design and response assessment.

## Funding

This study was supported by grants from the National Natural Science Foundation of China (No. 82471567, 81801757) and the Guangdong Basic and Applied Basic Research Foundation (No. 2024A1515010279, 2023A1515010256, 2022A 1515010369).

## Conflict of interest

The authors have no conflict of interests related to this publication.

## Author contributions

Conceptualization (LS, ZY), formal analysis (LS), methodology (LS, XL, XS, XZ, YD, BY), writing-original draft (LS, XS), data curation (XL, XZ, SZ), software (XL, FZ, YD), visualization (XS, SZ, BY), investigation (FZ), validation (ZY), writing-review & editing (ZY, RG), supervision (RG), resources (RG), and funding acquisition (RG). All authors made significant contributions to the study and approved the final manuscript.

## Ethical statement

All animal procedures and protocols were conducted in accordance with, and were approved by the Institutional Animal Care and Use Committee at the Third Affiliated Hospital of Sun Yat-Sen University and the Jennio Biotech Center (JENNIO-IACUC-2023-A014). In addition, reporting of the animal experiments followed the ARRIVE (Animal Research: Reporting of In Vivo Experiments) guidelines (https://arrive-guidelines.org/arrive-guidelines). All animals received human care.

## Data sharing statement

Data will be made available on request.

## References

[1] Sung H, Ferlay J, Siegel RL, Laversanne M, Soerjomataram I, Jemal A, *et*

*al*. Global Cancer Statistics 2020: GLOBOCAN Estimates of Incidence and Mortality Worldwide for 36 Cancers in 185 Countries. CA Cancer J Clin 2021;71(3):209–249. doi:10.3322/caac.21660, PMID:33538338.

[2] Vogel A, Meyer T, Sapisochin G, Salem R, Saborowski A. Hepatocellular carcinoma. Lancet 2022;400(10360):1345–1362. doi:10.1016/S0140-6736(22)01200-4, PMID:36084663.

[3] Sheta E, El-Kalla F, El-Gharib M, Kobtan A, Elhendawy M, Abd-Elsalam S, *et al*. Comparison of single-session transarterial chemoembolization combined with microwave ablation or radiofrequency ablation in the treatment of hepatocellular carcinoma: a randomized-controlled study. Eur J Gastroenterol Hepatol 2016;28(10):1198–1203. doi:10.1097/MEG.0000000000000688, PMID:27362551.

[4] Zhang YT, Xie MX, Wen J, Liang C, Song Q, Liu WX, *et al*. Hepatic TM6SF2 activates antitumour immunity to suppress metabolic dysfunction-associated steatotic liver disease-related hepatocellular carcinoma and boosts immunotherapy. Gut 2025;74(4):639–651. doi:10.1136/gutjnl-2024-333154, PMID:39667906.

[5] Li N, Zhu Y. Targeting liver cancer stem cells for the treatment of hepatocellular carcinoma. Ther Adv Gastroenterol 2019;12:1756284818821560. doi:10.1177/1756284818821560, PMID:30719075.

[6] Elhendawy M, Abdul-Baki EA, Abd-Elsalam S, Hagras MM, Zidan AA, Abdel-Naby AY, *et al*. MicroRNA signature in hepatocellular carcinoma patients: identification of potential markers. Mol Biol Rep 2020;47(7):4945–4953. doi:10.1007/s11033-020-05521-4, PMID:32430845.

[7] Hua S, Quan Y, Zhan M, Liao H, Li Y, Lu L. miR-125b-5p inhibits cell proliferation, migration, and invasion in hepatocellular carcinoma via targeting TXNRD1. Cancer Cell Int 2019;19:203. doi:10.1186/s12935-019-0919-6, PMID:31384178.

[8] Llovet JM, Montal R, Sia D, Finn RS. Molecular therapies and precision medicine for hepatocellular carcinoma. Nat Rev Clin Oncol 2018;15(10):599–616. doi:10.1038/s41571-018-0073-4, PMID:30061739.

[9] Mohammadi M, Jaafari MR, Mirzaei HR, Mirzaei H. Mesenchymal stem cell: a new horizon in cancer gene therapy. Cancer Gene Ther 2016;23(9):285–286. doi:10.1038/cgt.2016.35, PMID:27650780.

[10] Shi B, Wang Y, Zhao R, Long X, Deng W, Wang Z. Bone marrow mesenchymal stem cell-derived exosomal miR-21 protects C-kit+ cardiac stem cells from oxidative injury through the PTEN/PI3K/Akt axis. PLoS One 2018;13(2):e0191616. doi:10.1371/journal.pone.0191616, PMID:29444190.

[11] Wang Y, Yu C, Li Y, Bao H, Li X, Fan H, *et al*. In vivo MRI tracking and therapeutic efficacy of transplanted mesenchymal stem cells labeled with ferrimagnetic vortex iron oxide nanorings for liver fibrosis repair. Nanoscale 2022;14(13):5227–5238. doi:10.1039/d1nr08544a, PMID:35315848.

[12] Guo RM, Li QL, Luo ZX, Tang W, Jiao J, Wang J, *et al*. In Vivo Assessment of Neurodegeneration in Type C Niemann-Pick Disease by IDEAL-IQ. Korean J Radiol 2018;19(1):93–100. doi:10.3348/kjr.2018.19.1.93, PMID:29354005.

[13] Genove G, DeMarco U, Xu H, Goins WF, Ahrens ET. A new transgene reporter for in vivo magnetic resonance imaging. Nat Med 2005;11(4):450–454. doi:10.1038/nm1208, PMID:15778721.

[14] Zhang F, Duan X, Lu L, Zhang X, Chen M, Mao J, *et al*. In Vivo Long-Term Tracking of Neural Stem Cells Transplanted into an Acute Ischemic Stroke model with Reporter Gene-Based Bimodal MR and Optical Imaging. Cell Transplant 2017;26(10):1648–1662. doi:10.1177/0963689717722560, PMID:29251112.

[15] Gonçalves FG, Serai SD, Zuccoli G. Synthetic Brain MRI: Review of Current Concepts and Future Directions. Top Magn Reson Imaging 2018;27(6):387–393. doi:10.1097/RMR.0000000000000189, PMID:30516691.

[16] Zhu K, Chen Z, Cui L, Zhao J, Liu Y, Cao J. The Preoperative Diagnostic Performance of Multi-Parametric Quantitative Assessment in Rectal Carcinoma: A Preliminary Study Using Synthetic Magnetic Resonance Imaging. Front Oncol 2022;12:682003. doi:10.3389/fonc.2022.682003, PMID:35707367.

[17] Idilman IS, Yildiz AE, Karaosmanoglu AD, Ozmen MN, Akata D, Karcaaltincaba M. Proton density fat fraction: magnetic resonance imaging applications beyond the liver. Diagn Interv Radiol 2022;28(1):83–91. doi:10.5152/dir.2021.21845, PMID:35142615.

[18] Leslie J, Mackey JBG, Jamieson T, Ramon-Gil E, Drake TM, Fercoq F, *et al*. CXCR2 inhibition enables NASH-HCC immunotherapy. Gut 2022;71(10):2093–2106. doi:10.1136/gutjnl-2021-326259, PMID:35477863.

[19] Foerster F, Gairing SJ, Müller L, Galle PR. NAFLD-driven HCC: Safety and efficacy of current and emerging treatment options. J Hepatol 2022;76(2):446–457. doi:10.1016/j.jhep.2021.09.007, PMID:34555422.

[20] Pfister D, Núñez NG, Pinyol R, Govaere O, Pinter M, Szydlowska M, *et al*. NASH limits anti-tumour surveillance in immunotherapy-treated HCC. Nature 2021;592(7854):450–456. doi:10.1038/s41586-021-03362-0, PMID:33762733.

[21] Wu Y, Wang W, Chen Y, Huang K, Shuai X, Chen Q, *et al*. The investigation of polymer-siRNA nanoparticle for gene therapy of gastric cancer in vitro. Int J Nanomedicine 2010;5:129–136. doi:10.2147/ijn.s8503, PMID:20309399.

[22] Gao W, Yang Q, Li X, Chen X, Wei X, Diao Y, *et al*. Synthetic MRI with quantitative mappings for identifying receptor status, proliferation rate, and molecular subtypes of breast cancer. Eur J Radiol 2022;148:110168. doi:10.1016/j.ejrad.2022.110168, PMID:35078137.

[23] Yu G, Wang LG, Han Y, He QY. clusterProfiler: an R package for comparing biological themes among gene clusters. OMICS 2012;16(5):284–287. doi:10.1089/omi.2011.0118, PMID:22455463.

[24] Yu T, Li G, Wang C, Gong G, Wang L, Li C, *et al*. MIR210HG regulates glycolysis, cell proliferation, and metastasis of pancreatic cancer cells through miR-125b-5p/HK2/PKM2 axis. RNA Biol 2021;18(12):2513–2530. doi:10.1080/15476286.2021.1930755, PMID:34110962.

[25] Tian Z, Xu C, Yang P, Lin Z, Wu W, Zhang W, *et al*. Molecular pathogenesis: Connections between viral hepatitis-induced and non-alcoholic steatohepatitis-induced hepatocellular carcinoma. Front Immunol 2022;13:984728. doi:10.3389/fimmu.2022.984728, PMID:36189208.

[26] Li A, Wang R, Zhao Y, Zhao P, Yang J. Crosstalk between Epigenetics and Metabolic Reprogramming in Metabolic Dysfunction-Associated Steatotic Liver Disease-Induced Hepatocellular Carcinoma: A New Sight. Metabolites 2024;14(6):325. doi:10.3390/metabo14060325, PMID:38921460.

[27] Hui L, Zhang J, Guo X. MiR-125b-5p suppressed the glycolysis of laryngeal squamous cell carcinoma by down-regulating hexokinase-2. Biomed Pharmacother 2018;103:1194–1201. doi:10.1016/j.biopha.2018.04.098, PMID:29864898.

[28] Shi H, Li K, Feng J, Liu G, Feng Y, Zhang X. LncRNA-DANCR Interferes With miR-125b-5p/HK2 Axis to Desensitize Colon Cancer Cells to Cisplatin vis Activating Anaerobic Glycolysis. Front Oncol 2020;10:1034. doi:10.3389/fonc.2020.01034, PMID:32766131.

[29] An MX, Li S, Yao HB, Li C, Wang JM, Sun J, *et al*. BAG3 directly stabilizes Hexokinase 2 mRNA and promotes aerobic glycolysis in pancreatic cancer cells. J Cell Biol 2017;216(12):4091–4105. doi:10.1083/jcb.201701064, PMID:29114069.

[30] Wu X, Shen Y, Meng Y, Chen J, Zhang Y, Zeng S, *et al*. Suv39h1 contributes to activation of hepatic stellate cells in non-alcoholic fatty liver disease by enabling anaerobic glycolysis. Life Sci 2024;341:122498. doi:10.1016/j.lfs.2024.122498, PMID:38340980.

[31] Zhang CY, Tan XH, Yang HH, Jin L, Hong JR, Zhou Y, *et al*. COX-2/sEH Dual Inhibitor Alleviates Hepatocyte Senescence in NAFLD Mice by Restoring Autophagy through Sirt1/PI3K/AKT/mTOR. Int J Mol Sci 2022;23(15):8267. doi:10.3390/ijms23158267, PMID:35897843.

[32] Petito G, Giacco A, Cioffi F, Mazzoli A, Magnacca N, Iossa S, *et al*. Short-term fructose feeding alters tissue metabolic pathways by modulating microRNAs expression both in young and adult rats. Front Cell Dev Biol 2023;11:1101844. doi:10.3389/fcell.2023.1101844, PMID:36875756.

[33] Cai Q, Chen F, Xu F, Wang K, Zhang K, Li G, *et al*. Epigenetic silencing of microRNA-125b-5p promotes liver fibrosis in nonalcoholic fatty liver disease via integrin α8-mediated activation of RhoA signaling pathway. Metabolism 2020;104:154140. doi:10.1016/j.metabol.2020.154140, PMID:31926204.

[34] Rückerl D, Jenkins SJ, Laqtom NN, Gallagher IJ, Sutherland TE, Duncan S, *et al*. Induction of IL-4Rα-dependent microRNAs identifies PI3K/Akt signaling as essential for IL-4-driven murine macrophage proliferation in vivo. Blood 2012;120(11):2307–2316. doi:10.1182/blood-2012-02-408252, PMID:22855601.

[35] Jonas MI, Kuryłowicz A, Bartoszewicz Z, Lisik W, Jonas M, Kozniewski K, *et al*. Vitamin D Receptor Gene Expression in Adipose Tissue of Obese Individuals is Regulated by miRNA and Correlates with the Pro-Inflammatory Cytokine Level. Int J Mol Sci 2019;20(21):5272. doi:10.3390/ijms20215272, PMID:31652924.

[36] Lou G, Chen Z, Zheng M, Liu Y. Mesenchymal stem cell-derived exosomes as a new therapeutic strategy for liver diseases. Exp Mol Med 2017;49(6):e346. doi:10.1038/emm.2017.63, PMID:28620221.

[37] Rani S, Ryan AE, Griffin MD, Ritter T. Mesenchymal Stem Cell-derived Extracellular Vesicles: Toward Cell-free Therapeutic Applications. Mol Ther 2015;23(5):812–823. doi:10.1038/mt.2015.44, PMID:25868399.

[38] Kang M, Jordan V, Blenkiron C, Chamley LW. Biodistribution of extracellular vesicles following administration into animals: A systematic review. J Extracell Vesicles 2021;10(8):e12085. doi:10.1002/jev2.12085, PMID:34194679.

[39] Ferrini E, Stellari FF, Franceschi V, Macchi F, Russo L, Murgia A, *et al*. Persistency of Mesenchymal Stromal/Stem Cells in Lungs. Front Cell Dev Biol 2021;9:709225. doi:10.3389/fcell.2021.709225, PMID:34336863.

[40] Braid LR, Wood CA, Wiese DM, Ford BN. Intramuscular administration potentiates extended dwell time of mesenchymal stromal cells compared to other routes. Cytotherapy 2018;20(2):232–244. doi:10.1016/j.jcyt.2017.09.013, PMID:29167063.

[41] Afkhami H, Mahmoudvand G, Fakouri A, Shadab A, Mahjoor M, Komeili Movahhed T. New insights in application of mesenchymal stem cells therapy in tumor microenvironment: pros and cons. Front Cell Dev Biol 2023;11:1255697. doi:10.3389/fcell.2023.1255697, PMID:37849741.

[42] Watanabe T, Tsuchiya A, Takeuchi S, Nojiri S, Yoshida T, Ogawa M, *et al*. Development of a non-alcoholic steatohepatitis model with rapid accumulation of fibrosis, and its treatment using mesenchymal stem cells and their small extracellular vesicles. Regen Ther 2020;14:252–261. doi:10.1016/j.reth.2020.03.012, PMID:32455155.

[43] Arango-Rodriguez ML, Ezquer F, Ezquer M, Conget P. Could cancer and infection be adverse effects of mesenchymal stromal cell therapy? World J Stem Cells 2015;7(2):408–417. doi:10.4252/wjsc.v7.i2.408, PMID:25815124.

[44] Nicodemou A, Bernátová S, Čeháková M, Danišovič Ľ. Emerging Roles of Mesenchymal Stem/Stromal-Cell-Derived Extracellular Vesicles in Cancer Therapy. Pharmaceutics 2023;15(5):1453. doi:10.3390/pharmaceutics15051453, PMID:37242693.

[45] Liu T, Zhu Y, Zhao R, Wei X, Xin X. Visualization of exosomes from mesenchymal stem cells in vivo by magnetic resonance imaging. Magn Reson Imaging 2020;68:75–82. doi:10.1016/j.mri.2020.02.001, PMID:32027941.

[46] Yang C, Tian R, Liu T, Liu G. MRI Reporter Genes for Noninvasive Molecular Imaging. Molecules 2016;21(5):580. doi:10.3390/molecules21050580, PMID:27213309.

[47] Cheng S, Mi R, Xu Y, Jin G, Zhang J, Zhou Y, *et al*. Ferritin heavy chain as a molecular imaging reporter gene in glioma xenografts. J Cancer

Res Clin Oncol 2017;143(6):941–951. doi:10.1007/s00432-017-2356-z, PMID:28247036.

[48] Li Q, Xiao Q, Yang M, Chai Q, Huang Y, Wu PY, *et al*. Histogram analysis of quantitative parameters from synthetic MRI: Correlations with prognostic factors and molecular subtypes in invasive ductal breast cancer. Eur J Radiol 2021;139:109697. doi:10.1016/j.ejrad.2021.109697, PMID:33857828.

[49] Lescher S, Jurcoane A, Veit A, Bähr O, Deichmann R, Hattingen E. Quantitative T1 and T2 mapping in recurrent glioblastomas under bevacizumab: earlier detection of tumor progression compared to conventional MRI. Neuroradiology 2015;57(1):11–20. doi:10.1007/s00234-014-1445-9, PMID:25287076.

[50] Wang X, Zhang L, Dong B. Molecular mechanisms in MASLD/MASH-related HCC. Hepatology 2025;82(5):1303–1324. doi:10.1097/HEP.0000000000000786, PMID:38349726.